Viscoplastic tearing of polyethylene thin film

Dezso Hegyi & Sergio Pellegrino

Mechanics of Time-Dependent Materials
An International Journal Devoted to the Time-Dependent Behaviour of Materials and Structures

ISSN 1385-2000
Volume 19
Number 2

Mech Time-Depend Mater (2015)
19:187-208
DOI 10.1007/s11043-015-9259-7

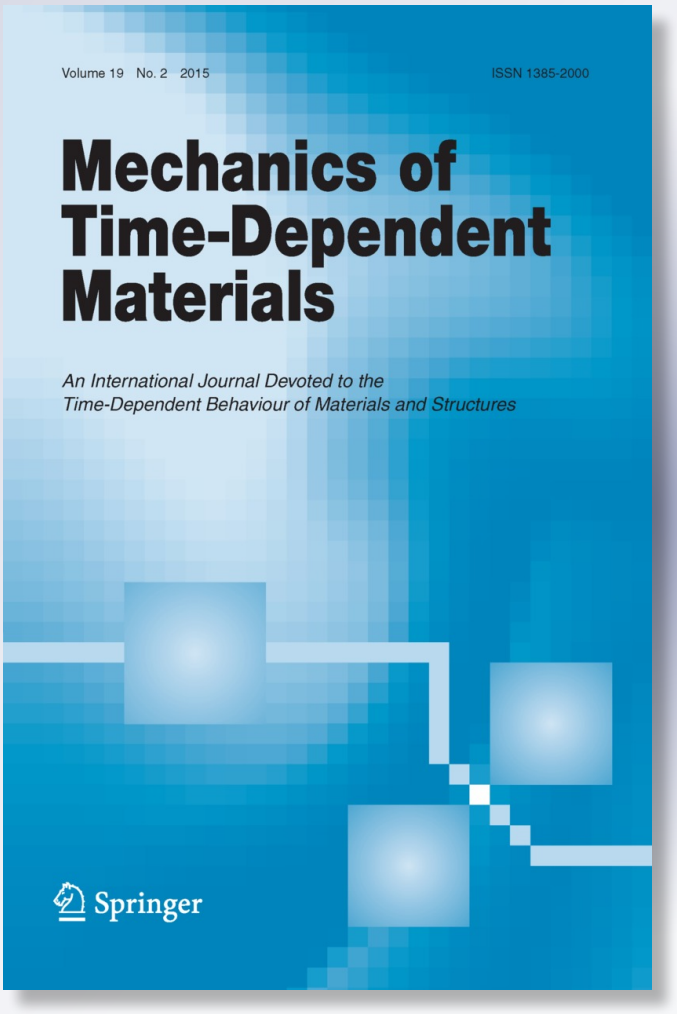

Springer

Your article is protected by copyright and all rights are held exclusively by Springer Science +Business Media Dordrecht. This e-offprint is for personal use only and shall not be self-archived in electronic repositories. If you wish to self-archive your article, please use the accepted manuscript version for posting on your own website. You may further deposit the accepted manuscript version in any repository, provided it is only made publicly available 12 months after official publication or later and provided acknowledgement is given to the original source of publication and a link is inserted to the published article on Springer's website. The link must be accompanied by the following text: "The final publication is available at link.springer.com".

Author's personal copy

Mech Time-Depend Mater (2015) 19:187–208
DOI 10.1007/s11043-015-9259-7

Viscoplastic tearing of polyethylene thin film

Dezso Hegyi[1] **· Sergio Pellegrino**[2]

Received: 31 January 2014 / Accepted: 19 February 2015 / Published online: 27 March 2015
© Springer Science+Business Media Dordrecht 2015

Abstract Recent advances in noncontact strain measurement techniques and large-strain constitutive modeling of the linear low-density polyethylene film used in NASA superpressure balloons StratoFilm 420 are combined to provide a novel measurement technique for the tear propagation critical value of the J-integral. Previously these measurements required complex test configurations and procedures. It is found that the critical value of the J-integral increases by approximately 50 % when the strain rate is decreased from 1.33×10^{-4} s^{-1} to 1.33×10^{-5} s^{-1}. It is shown that there is good correlation between measurements made on uniaxially loaded dogbone samples and circular diaphragms loaded by pressure, both with a 2-mm-wide slit in the middle. This result indicates that more extensive studies of strain-rate dependence may be made with the simpler, uniaxial test configuration.

Keywords Viscoelasticity · Free volume model · J-integral · StratoFilm

1 Introduction

The use of linear low-density polyethylene (LLDPE) films in NASA superpressure balloons has motivated extensive studies of their viscoelastic behavior in the small and large strain regimes. However, their viscoplastic behavior and ultimate failure have remained relatively unexplored, making it difficult to quantify the failure margins of structures built from these films. Currently, balloon designers are forced to the conservatism of point-based stress failure criteria. The objective of the present study is to gain insight into the viscoplastic tearing

✉ S. Pellegrino
sergiop@caltech.edu

D. Hegyi
dizso@szt.bme.hu

1 Department of Mechanics, Materials and Structures, Budapest University of Technology and Economics, Müegyetem rkp. 3, 1111 Budapest, Hungary

2 Graduate Aerospace Laboratories, California Institute of Technology, 1200 E. California Blvd., Pasadena, CA 91125, USA

Author's personal copy

of LLDPE films and to develop quantitative models that in the future will enable more rational estimates of load margins.

Essential background for the present study is the recent development of viscoelastic models (Rand 2008; Kwok and Pellegrino 2011; Kwok 2012; Li et al. 2015) for LLDPE films. Balloon designers are currently using these models, in combination with stress limits based on a 2 % strain offset, to provide a failure criterion for balloon film. However, such an approach may be overly conservative in the case of localized stress peaks, and yet the possibility of slowly propagating tears in films loaded over long periods of time is neglected. Pointwise failure criteria neglect the stress redistribution that occurs near a peak and thus may underestimate the reserve strength of a structure. A global approach that allows the stresses to redistribute until the occurrence of macroscopic yielding or tearing of the film occur, required to estimate the full strength.

Failure of polymers is frequently approached with time-dependent yield criteria expressed in terms of stress components or energy. These criteria are able to capture the time to failure of the polymer. Key references on this general topic include (Knauss 1989; Brown and Lu 1995; Brinson and Brinson 2008), but there has been no specific study of the time to failure of LLDPE film. Tielking (1993) has argued that the critical value of the integral of the energy release rate on a closed path that surrounds the tip of a small slit (J-integral) in a thin film can be measured only in a plane-strain biaxial test, and hence carried out a series of complex tests on wide rectangular samples to obtain the relationship between crack amplitude and the J-integral.

For highly ductile, soft materials, the essential work method (Chan and Williams 1994) measures the work done by the test machine on tensile samples with double-edged notches in the middle. This test geometry provides a fully plastic area in a narrow ligament, whereas most of the sample remains elastic. It has been argued that the essential work method is equivalent to the J-integral and yet is easier to implement in soft materials; however, its performance for thin films is not known.

The present study builds on recent advances in experimental techniques, particularly in 3D digital image correlation (DIC), and on large-strain constitutive modeling of LLDPE thin films, to obtain the critical values of the J-integral from direct strain measurements on two different sample geometries. Both uniaxial tension and biaxial pressure-load tests are considered. It is found that the test configuration has only rather minor effects on the critical value of the J-integral J_c, which suggests that it is possible to obtain this key property from the simpler of the two configurations. An additional advantage of measuring J_c from the simpler, uniaxial test samples is that in this case it is possible to control strain rate effects directly. These results provide the background and a methodology for the future development of detailed tearing criteria for LLDPE films.

The paper is laid out as follows. Section 2 presents a brief review of linear viscoelasticity, followed by a nonlinear viscoelastic model for LLDPE thin films and by a review of the literature on time-dependent failure of polymers. Section 3 presents a set of preliminary uniaxial tension tests on dogbone samples of LDDPE film to select the best length of the slit. Section 4 presents two test configurations, dogbone and spherical, in which the expansion and propagation of 2-mm-wide transverse cracks were measured. Section 5 presents the analysis method to compute the stress field and the strain energy distribution, and Sect. 6 presents the results of the J-integral computations for different test configurations. Section 7 discusses the key results of the paper and concludes that there is a good correlation between the values of J_c for the two different sample geometries.

Author's personal copy

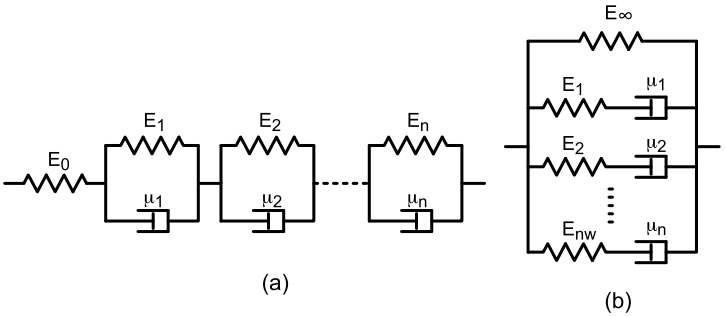

Fig. 1 (**a**) Kelvin–Voigt elements in series provide a creep model; (**b**) Maxwell elements in parallel provide a relaxation model

2 Background to time-dependent behavior

2.1 Linear viscoelastic models

The uniaxial time-dependent behavior of polymers can be described by combinations of springs and dampers (Coleman and Noll 1961; Christensen 1982; Ferry 1980; Flugge and Viscoelasticity 1975). To model creep a series of n Kelvin–Voigt elements is typically used (see Fig. 1(a)), and the corresponding expression for the time-dependent compliance $D_{(t)}$ using a Prony series is

$$D_{(t)} = D_0 + \sum_{i=1}^{n} D_i \cdot \left(1 - e^{-t/\tau_i}\right), \tag{1}$$

where t is the time variable, D_0 is the compliance at time 0, D_i is the compliance, and τ_i is the retardation time for the ith element.

To model relaxation a series of Maxwell elements in parallel is typically used (see Fig. 1(b)), and the corresponding expression for the relaxation modulus $E_{(t)}$ is

$$E_{(t)} = E_\infty + \sum_{i=1}^{n} E_i \cdot e^{-t/\rho_i}, \tag{2}$$

where E_∞ is the long-term modulus, E_i is the stiffness, and ρ_i is the relaxation time for the ith element.

In these models, element i corresponds to a specific term in the Prony series in Eqs. (1)–(2). The coefficients of the Prony series correspond to the parameters of the springs and dampers, with viscosity μ_i, in the physical models.

Temperature and time effects are combined through the time–temperature superposition (TTS) principle (Brinson and Brinson 2008), which states that for a class of materials known as thermorheologically simple, varying the temperature provides a logarithmic correction to the real time scale t. Hence, a reduced time t' is defined, which is related to real time by

$$t' = \frac{t}{a_T}. \tag{3}$$

Here the time shift factor a_t is determined experimentally and is usually assumed to have the expression (Williams et al. 1955)

$$\log a_T = -\frac{c_1 \cdot (T - T_0)}{c_2 + (T - T_0)}. \tag{4}$$

Author's personal copy

Note that the logarithm is in base 10. Also, T is the actual temperature, and T_0 is the reference temperature at which the material characterization tests were carried out. The material constants c_1 and c_2 are obtained by fitting Eq. (4) to experimental measurements.

The time-dependent stress and strain can be computed by stepping over time using the constitutive model as follows. Consider Fig. 1(a) and note that the Kelvin–Voigt elements are in series, hence the stress σ_t is equal throughout, and so

$$\sigma_t = \epsilon_0 \cdot E_0 = \epsilon_{it} \cdot E_i + \mu_i \cdot \frac{d\epsilon_{it}}{dt}, \tag{5}$$

where the subscript t, without brackets, denotes the value calculated at time step t.

The overall strain in the Kelvin–Voigt model is obtained by adding the strain in each element, and hence

$$\epsilon_t = \epsilon_{0t} + \sum_{i=1}^{n} \epsilon_{it}. \tag{6}$$

Both of these equations can be written in incremental form to allow the calculation of stress and strain at time t when their values at the previous time step $t-1$ are known. The incremental form of Eq. (5) is

$$\sigma_t = (\epsilon_{it-1} + d\epsilon_i) \cdot E_i + \mu_i \cdot \frac{d\epsilon_i}{dt}, \tag{7}$$

which can be rearranged to

$$d\epsilon_i \cdot \left(E_i + \frac{\mu_i}{dt} \right) - \sigma_t = -\epsilon_{it-1} \cdot E_i. \tag{8}$$

The incremental form of Eq. (6) is

$$d\epsilon_{0t} + \sum_{i=1}^{n} d\epsilon_t = \epsilon_t - \epsilon_{0t-1} - \sum_{i=1}^{n} \epsilon_{it-1}. \tag{9}$$

Given the strain in each element at time $t-1$, ϵ_{it-1}, and the total strain at time t, ϵ_t, together with the Prony coefficients, the strain increments in each element $d\epsilon_i$ and the common stress σ_t can be calculated by solving a system of $n+1$ linear equations.

2.2 Large-strain viscoelastic model for StratoFilm 420

The particular LLDPE film studied in this paper is the 38-μm-thick film used in the NASA superpressure balloons; this film is called StratoFilm 420 (Rand and Wakefield 2010).

To capture large strain viscoelasticity, instead of Eq. (4), the alternative expression for the shift factor proposed by Knauss and Emri (1981), Knauss and Emri (1987) is adopted:

$$\log a_T = -\frac{B}{2.303 f_0} \left(\frac{\alpha_V (T - T_0) + \epsilon_V}{f_0 + \alpha_V (T - T_0) + \epsilon_V} \right). \tag{10}$$

Note that Eq. (10) incorporates the volumetric strain of the material in order to account for strain-related changes in the mobility of molecular chains; ϵ_V is the volumetric strain, and α_V is the volumetric coefficient of thermal expansion.

The volumetric strain ϵ_V has the following expression in terms of the Green–Lagrange strain components, where 1 and 2 are the in-plane directions of orthotropy (respectively in the machine and transverse direction of the film), and 3 is the through-thickness direction:

$$\epsilon_V \cong \sqrt{2\epsilon_{11} + 1} \cdot \sqrt{2\epsilon_{22} + 1} \cdot \sqrt{2\epsilon_{33} + 1} - 1, \tag{11}$$

Author's personal copy

Table 1 Thermal expansion parameters for StratoFilm420

j	p_{1j} [K^{-1}]	p_{2j} [K^{-1}]
1	$-1.314349420165660 \cdot 10^{-27}$	$1.656628670569420 \cdot 10^{-27}$
2	$3.757961363054510 \cdot 10^{-24}$	$-4.538552920810370 \cdot 10^{-24}$
3	$-4.870560919889060 \cdot 10^{-21}$	$5.644504822368260 \cdot 10^{-21}$
4	$3.783161974578100 \cdot 10^{-18}$	$-4.213294503544060 \cdot 10^{-18}$
5	$-1.961126506078030 \cdot 10^{-15}$	$2.102008465628270 \cdot 10^{-15}$
6	$7.146793667601330 \cdot 10^{-13}$	$-7.383200108461120 \cdot 10^{-13}$
7	$-1.877228425197230 \cdot 10^{-10}$	$1.871956621022750 \cdot 10^{-10}$
8	$3.580706769622300 \cdot 10^{-8}$	$-3.451673660888610 \cdot 10^{-8}$
9	$-4.922242452967390 \cdot 10^{-6}$	$4.593443382129490 \cdot 10^{-6}$
10	$4.755521948988130 \cdot 10^{-4}$	$-4.302432036460990 \cdot 10^{-4}$
11	$-3.065068396780760 \cdot 10^{-2}$	$2.692250002443280 \cdot 10^{-2}$
12	$1.183350730959610 \cdot 10^{0}$	$-1.010550330725230 \cdot 10^{0}$
13	$-2.069690662157120 \cdot 10^{1}$	$1.720772480526920 \cdot 10^{1}$

α_V can be calculated from the linear coefficients of thermal expansion:

$$\alpha_V \cong \alpha_1 + \alpha_2 + \alpha_3. \tag{12}$$

The in-plane coefficients of thermal expansion α_1 and α_2 were measured by Young (2010), who provided the following polynomial expressions, valid in the range 170–320 K:

$$\alpha_i = \sum_{j=1}^{13} p_{ij} T^{13-j} \quad \text{for } i = 1, 2, \tag{13}$$

where the parameters p_{ij} are provided in Table 1.

Li et al. (2015) have shown that equally accurate large strain models can be set up for different expressions of α_3; hence, it is easiest to assume that

$$\alpha_3 = 0. \tag{14}$$

Thin films are subject to plane stress conditions, and hence the creep compliance is usually expressed as a 3 by 3 matrix that relates the in-plane stress and strain component (Rand 2008).

However, in the present study, ϵ_{33} is additionally needed to compute the volumetric strain, and hence a 4 by 4 compliance matrix is defined:

$$\begin{bmatrix} D_{11(t)} & D_{12(t)} & D_{13(t)} & 0 \\ D_{12(t)} & D_{22(t)} & D_{23(t)} & 0 \\ D_{13(t)} & D_{23(t)} & D_{33(t)} & 0 \\ 0 & 0 & 0 & D_{66(t)} \end{bmatrix}, \tag{15}$$

where D_{66} is the in-plane shear compliance. A plot of D_{11} is shown in Fig. 2.

Li et al. (2015) have recently derived from creep tests the following parameters for the time shift factor in Eq. (10):

$$B = 1610 \quad \text{and} \quad f_0 = 1.752, \tag{16}$$

as well as the in-plane creep compliance coefficients D_{11}, D_{22}, D_{12}, provided in Table 2. The out-of-plane coefficients D_{13} and D_{23}, also provided in the table, were obtained by

Author's personal copy

Table 2 Parameters of compliance Prony series for StratoFilm 420

i	τ [s]	D_{11} [MPa^{-1}]	D_{22} [MPa^{-1}]	$-D_{12}$ [MPa^{-1}]	D_{13} [MPa^{-1}]	D_{23} [MPa^{-1}]
0	0	$3.0 \cdot 10^{-4}$	$3.0 \cdot 10^{-4}$	$1.5 \cdot 10^{-4}$	$-8.020578 \cdot 10^{-5}$	$-2.489835 \cdot 10^{-5}$
1	$1.0 \cdot 10^{-9}$	$1.742744 \cdot 10^{-4}$	$1.099837 \cdot 10^{-4}$	$6.173672 \cdot 10^{-6}$	$1.417732 \cdot 10^{-5}$	$-1.486979 \cdot 10^{-5}$
2	$1.0 \cdot 10^{-8}$	$6.510906 \cdot 10^{-6}$	$5.864904 \cdot 10^{-5}$	$2.739557 \cdot 10^{-5}$	$-2.989882 \cdot 10^{-5}$	$-6.915666 \cdot 10^{-5}$
3	$1.0 \cdot 10^{-7}$	$6.284269 \cdot 10^{-5}$	$2.414277 \cdot 10^{-5}$	$5.169134 \cdot 10^{-5}$	$4.949892 \cdot 10^{-5}$	$-9.152935 \cdot 10^{-6}$
4	$1.0 \cdot 10^{-6}$	$1.075431 \cdot 10^{-4}$	$4.221770 \cdot 10^{-5}$	$5.750443 \cdot 10^{-5}$	$-4.295294 \cdot 10^{-5}$	$3.786862 \cdot 10^{-5}$
5	$1.0 \cdot 10^{-5}$	$5.857710 \cdot 10^{-5}$	$1.506274 \cdot 10^{-4}$	$9.245293 \cdot 10^{-6}$	$1.656885 \cdot 10^{-4}$	$1.107330 \cdot 10^{-4}$
6	$1.0 \cdot 10^{-4}$	$1.550803 \cdot 10^{-4}$	$9.609312 \cdot 10^{-5}$	$1.315824 \cdot 10^{-4}$	$1.574928 \cdot 10^{-5}$	$3.056652 \cdot 10^{-5}$
7	$1.0 \cdot 10^{-3}$	$2.843866 \cdot 10^{-4}$	$2.597968 \cdot 10^{-4}$	$1.954518 \cdot 10^{-4}$	$-7.100409 \cdot 10^{-5}$	$-9.308906 \cdot 10^{-6}$
8	$1.0 \cdot 10^{-2}$	$4.567155 \cdot 10^{-4}$	$4.462205 \cdot 10^{-4}$	$2.426414 \cdot 10^{-4}$	$-5.967733 \cdot 10^{-5}$	$-1.172953 \cdot 10^{-4}$
9	$1.0 \cdot 10^{-1}$	$6.461394 \cdot 10^{-4}$	$4.793379 \cdot 10^{-4}$	$3.909654 \cdot 10^{-4}$	$-1.651097 \cdot 10^{-4}$	$6.069053 \cdot 10^{-5}$
10	$1.0 \cdot 10^{0}$	$8.698046 \cdot 10^{-4}$	$5.911529 \cdot 10^{-4}$	$5.343249 \cdot 10^{-4}$	$-7.618915 \cdot 10^{-5}$	$8.091049 \cdot 10^{-5}$
11	$1.0 \cdot 10^{+1}$	$1.017441 \cdot 10^{-3}$	$7.511220 \cdot 10^{-4}$	$6.859082 \cdot 10^{-4}$	$-3.185557 \cdot 10^{-4}$	$-2.022027 \cdot 10^{-5}$
12	$1.0 \cdot 10^{+2}$	$1.120139 \cdot 10^{-3}$	$1.237382 \cdot 10^{-3}$	$6.414569 \cdot 10^{-4}$	$-3.834378 \cdot 10^{-5}$	$-4.021026 \cdot 10^{-4}$
13	$1.0 \cdot 10^{+3}$	$1.088133 \cdot 10^{-3}$	$1.262248 \cdot 10^{-3}$	$5.781361 \cdot 10^{-4}$	$-1.826515 \cdot 10^{-4}$	$-2.684576 \cdot 10^{-4}$
14	$1.0 \cdot 10^{+4}$	$8.624522 \cdot 10^{-4}$	$6.440784 \cdot 10^{-4}$	$6.454454 \cdot 10^{-4}$	$2.793315 \cdot 10^{-4}$	$5.106999 \cdot 10^{-4}$
15	$1.0 \cdot 10^{+5}$	$1.059337 \cdot 10^{-3}$	$8.245951 \cdot 10^{-4}$	$6.162569 \cdot 10^{-4}$	$-7.470997 \cdot 10^{-6}$	$-4.664092 \cdot 10^{-5}$
16	$1.0 \cdot 10^{+6}$	$1.149470 \cdot 10^{-3}$	$9.435898 \cdot 10^{-4}$	$6.142091 \cdot 10^{-4}$	$-1.867866 \cdot 10^{-4}$	$-1.068666 \cdot 10^{-4}$
17	$1.0 \cdot 10^{+7}$	$1.414411 \cdot 10^{-3}$	$1.742152 \cdot 10^{-3}$	$1.049955 \cdot 10^{-3}$	$-1.028044 \cdot 10^{-4}$	$-6.341502 \cdot 10^{-4}$
18	$1.0 \cdot 10^{+8}$	$9.262340 \cdot 10^{-4}$	$7.797793 \cdot 10^{-4}$	$5.307633 \cdot 10^{-4}$	$-7.175202 \cdot 10^{-6}$	$-2.024296 \cdot 10^{-4}$
19	$1.0 \cdot 10^{+9}$	$1.370308 \cdot 10^{-4}$	$9.743801 \cdot 10^{-5}$	$6.842945 \cdot 10^{-5}$	$2.356255 \cdot 10^{-5}$	$-7.689222 \cdot 10^{-6}$

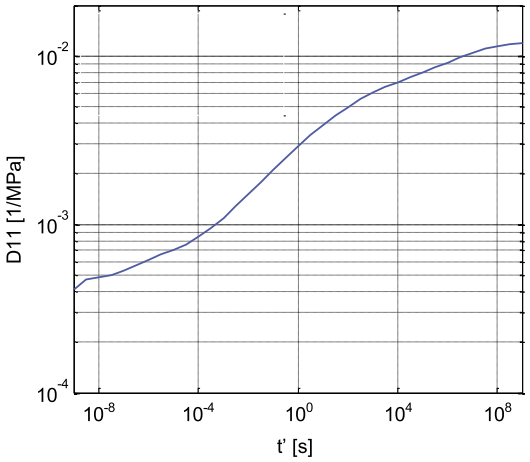

Fig. 2 Compliance master curve for StratoFilm 420 in machine direction at 293 K (Kwok 2012)

considering the measured in-plane nonlinear behavior in combination with the nonlinear model. Following (Rand 2008), $D_{66} = 4.48 \times D_{11}$. The last coefficient of the compliance matrix D_{33} is not needed; more details will be provided in Sect. 5. Note that the creep compliance coefficients of StratoFilm420 indicate a mildly orthotropic behavior, whereas the thermal expansion coefficients are strongly orthotropic.

Author's personal copy

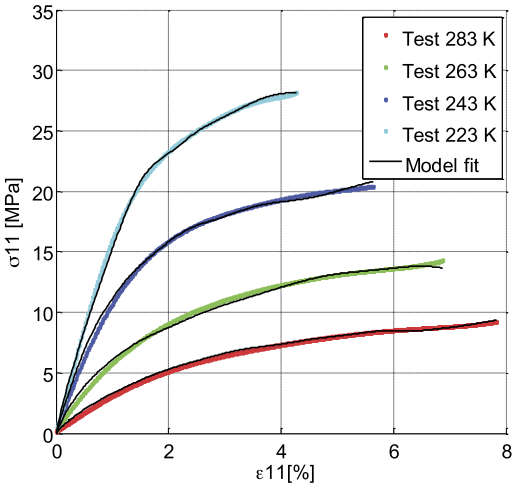

Fig. 3 Comparison of experimentally measured stress–strain behavior at four temperatures, with predictions from large strain model, at a uniform strain rate of 0.1 % s^{-1}

This large-strain model has been shown to be accurate up to the point of horizontal tangency in the stress–strain curve. This point marks the onset of nonrecoverable deformation for the film. For example, at 263 K and a strain rate of 0.1 % s^{-1}, nonrecoverable deformation becomes significant at a strain in excess of 7 %; see Fig. 3. Until this strain value is reached, the measured and predicted stress–strain relationship are practically coincident. At lower temperature, the measured and predicted relationships are also practically coincident, although the strain limit is lower.

2.3 Failure of polymer films

Uncrosslinked polymers such as LLDPE are used mainly above the glass transition temperature (T_g), to avoid brittle behavior. Hence, under normal operating conditions, they can show significant time-dependent deformation and plasticity. Their failure behavior also depends on time and temperature. For example, a test sample that is loaded well below the failure load measured at room temperature in a short-duration test may fail when the same load is applied for a longer period of time. Also, at lower temperature, the strength of the sample increases.

The prediction of failure for such materials has been modeled by defining a function (failure criterion) that relates stress, strain, and several other time-dependent parameters to a time-dependent yield stress. One approach (Naghdi and Murch 1963; Crochet 1966) considers the function

$$f = \frac{1}{2}\sigma_{ij}\sigma_{ij} - \left(A + B\exp\left(-C\sqrt{\left(\epsilon_{ij}^{V} - \epsilon_{ij}^{E}\right)\cdot\left(\epsilon_{ij}^{V} - \epsilon_{ij}^{E}\right)}\right)\right)^2 = 0, \tag{17}$$

where σ_{ij} is the stress tensor, ϵ_{ij} is the strain tensor, and the superscripts V and E denote viscous and elastic components. Note that Eq. (17) is defined in terms of a Mises equivalent stress (first term) and a time-dependent yield stress (second term); A, B, and C are material parameters.

In an alternative approach, it has been assumed that failure is linked to the stored strain energy reaching a critical level, without accounting for viscous or plastically dissipated energy (Bruler 1973; Bruler 1981; Brinson 1999). Furthermore, only the deviatoric component of the strain energy is considered, not the dilatational energy. Since the time-dependent stress

Author's personal copy

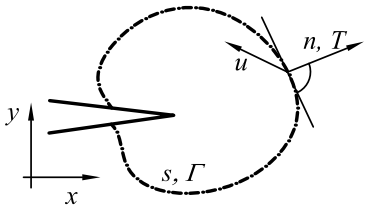

Fig. 4 Integration path around crack tip

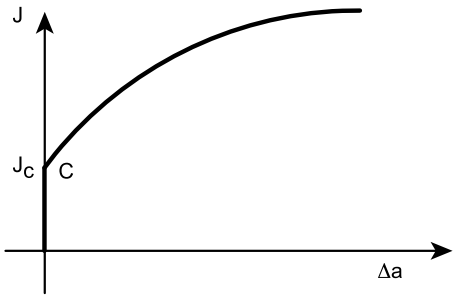

Fig. 5 Schematic diagram of relationship between J-integral and increase of crack length Δa. J_c marks the start of the crack propagation

and strain components can be estimated from a finite element analysis, implementation of the latter approach requires only a single failure parameter to be defined, and hence it is simpler to implement this approach than the three-parameter criterion in Eq. (17).

A different approach to the failure of polymer films relates failure to the propagation of a crack (Tielking 1993) and adopts fracture mechanics tools to study this problem. The J-integral is the integral of the energy release rate on a path Γ that surrounds the crack tip; in elastic fracture mechanics, it is path independent and is equal to the energy release rate, that is, the fracture energy per unit surface of crack (Rice and Rosengren 1968); see Fig. 4. It can be calculated from

$$J = \int_{\Gamma} \left(W n_1 - T \frac{\partial u}{\partial x} \right) ds, \tag{18}$$

where W is the strain energy density, n_1 is the normal strain n in the direction of the normal to Γ, T is the normal stress in the n-direction, u is the displacement of a general point, the x-axis is defined parallel to the direction of propagation of the crack, and ds is an infinitesimal element along Γ.

The J-integral is usually plotted as a function of the crack length increase Δa, see Fig. 5, where J_c is the critical value of J when the crack size starts to increase. The slope of the J-curve beyond J_c indicates the resistance of the material to crack propagation.

In isotropic elastic materials of modulus E and under plane stress, the toughness K is directly related to the energy release rate G and to J by

$$\frac{K^2}{E} = G = J. \tag{19}$$

In the case of inelastic materials, a part of the energy is dissipated, but the J-integral still gives a general method to determine the energy release associated with the crack propagation and can be determined by using the stress–strain relation far from the crack-disturbed area.

Tielking (1993) carried out unidirectional load tests on 76-mm-long and 254-mm-wide samples of 20-μm-thick StratoFilm. Because of the large width-to-length ratio of these sam-

Author's personal copy

Table 3 Results of preliminary failure tests. Temperature, humidity, rate, yield stress (f_y), breaking stress (f_u), ultimate extension (u_u)

	Test 1: no hole				Test 2: pinhole		Test 3: slit			
Temp. [K]	263	263	223	223	223	223	223	223	223	203
Humidity [%]	75	85	40	40	40	40	40	40	20	20
Rate [mm/s]	0.1	0.2	0.1	0.2	0.1	0.2	0.1	0.01	0.001	0.001
f_y [N/mm^2]	16	15	24	26	26	26	22	26	26	34
f_u [N/mm^2]	17	16	26	26	22	24	22	26	26	34
u_u [mm]	190	210	100	110	60	35	3	3	3	2.5

ples, the effect of their edge deformation on crack propagation was negligible, and hence the J-integral can be evaluated indirectly from the equation (Begley and Landes 1972)

$$J = \frac{1}{B}\frac{\partial W_T}{\partial a}, \tag{20}$$

where B is the thickness of the sample, W_T is the total work of the loading mechanism, and a is the half length of the crack.

Tielking carried out multiple loading–unloading cycles and evaluated J using this equation; each point of the J–Δa diagram was determined from the difference between the loading–unloading energies and the change in Δa.

3 Failure by viscoelastic tearing: preliminary tests

For an initial understanding of the failure of StratoFilm 420, preliminary tests were carried out on 75-mm-long and 12-mm-wide laser-cut dogbone samples, with the direction of extrusion of the film (machine direction) aligned with the longer dimension of the sample. These tests investigated the difference in behavior between pristine film vs. film damaged by introducing a pinhole or a small slit.

The tests were carried out in an Instron 3119-506 environmental chamber at temperatures between 203 K and 263 K using an Instron 5569 electromechanical materials testing machine. The ultimate strength f_u was determined from the peak in the load-extension diagram generated by the Instron BlueHill software. The yield stress f_y was determined by the point of intersection between a tangent line at the origin and a tangent to the initially nonlinear part of the diagram. The ultimate extension u_u was determined from the last measured point. The full set of results is presented in Table 3. Note that, in the case of samples that failed after extensive plastic deformation, f_y and f_u refer to the original cross-section and hence do not reflect the true stress state in the necked sample. Representative snapshots from each set of tests are shown in Fig. 6(a–d), and the load-extension plots for four representative tests are presented in Fig. 6(e).

The first set of tests (Test 1) was carried out on pristine samples. Tests at two different strain rates, 1.33×10^{-3} s^{-1} and 2.66×10^{-3} s^{-1}, and two different temperatures, 263 K and 223 K, on 6-mm and 12-mm-wide samples showed large stretching (100–300 %) followed by the formation of a neck and failure of the sample. In all of these tests, there was a significant amount of plastic deformation, as evidenced by the milky appearance of the sample (crazing). In the higher-temperature (263 K) tests, crazing developed over the full length of the samples. In the lower-temperature (223 K) tests, crazing started at one end of

Author's personal copy

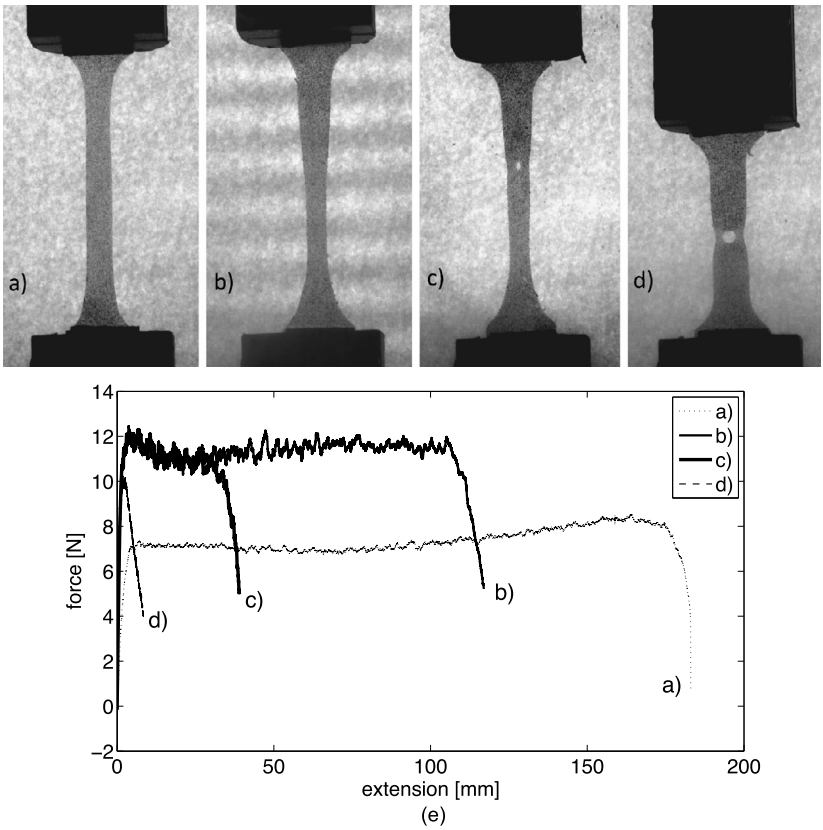

Fig. 6 Snapshots from four tests on dogbone samples with initial width of 12 mm: (**a**) no hole, $T = 263$ K; (**b**) no hole, $T = 223$ K, (**c**) pinhole, $T = 223$ K; (**d**) 2-mm-wide slit, $T = 223$ K; (**e**) force-extension diagrams for the four tests

the sample (in the case shown in Fig. 6(b), crazing started at the bottom) and propagated through the full length of the sample before necking began. The ultimate stress was higher at the lower temperature and at the higher strain rate. This type of behavior is described with good accuracy by the energy-based failure criteria in Sect. 2.3, apart from the need to account for the large elongation before failure. The observed dependence of the ultimate stress on temperature is also captured by this approach.

The second set of tests (Test 2) was carried out on samples that had been initially damaged by introducing a pinhole in the middle. The idea for this test, which was done only at the lower temperature of 223 K, was that the pinhole might provide the initiation point for a tear through the sample, avoiding a large amount of crazing. However, extensive crazing was still observed in this set of tests. Crazing always started at a point away from the pinhole, usually near one end of the sample, and propagated through the sample until it reached the pinhole. At this point, the sample broke by propagation of a tear. The measured ultimate strength was in the same range as in the tests without pinhole, but this time the ultimate extension of the sample was significantly smaller; see Fig. 6(e). Hence, it was concluded that a pinhole has no appreciable effect on the global strength, but it does affect the maximum global deformation.

Author's personal copy

The third set of tests (Test 3) was carried out on samples with a central 2 mm transversal slit. In this case, crazing first appeared near the tips of the slit, which rapidly expanded and tore through the sample. The ultimate extension was much smaller than in the previous two cases; see curve (d) in Fig. 6(e); however, the ultimate strength values were in the same range as for the other types of samples.

The tests on pristine samples showed a large amount of visco-plastic deformation. Lower temperatures caused the strength to increase, as expected from the failure criterion approach in Sect. 2.3. However, doubling the strain rate did not increase the strength as predicted by the failure criterion. Introducing a pinhole or a slit in the sample did not change the overall strength, but it substantially decreased the ultimate elongation.

These results were useful in planning further, more detailed experiments. Since all three sample configurations had provided approximately the same ultimate strength, the choice between pristine, damaged by a pinhole, or damaged by a slit was made on the basis of which configuration is most suited to producing the highest resolution in the strain field near the crack that ultimately tears through the sample. This strain field can be used to evaluate the J-integral around the crack. Here the key factor is the limited viewing field over which DIC systems can produce high-resolution strain fields. In order to image a narrow region of the sample and to avoid that this region moves out of the viewing field during the test, the third sample configuration was selected.

4 Test apparatus and sample configurations

The strain in the film was measured with the Correlated Solutions Vic-3D 2010 DIC system. Three-dimensional DIC captures the effects of out-of-plane deformations, including any wrinkling of the film. The test configuration can be seen in Fig. 7; the cameras were Point Gray GRAS-50SSM-C with Pentax 75-mm F/2.8 lenses, set up with a field of view of approximately 50 mm. The test samples were lightly sprayed with black paint to provide a random speckle pattern with average size of 0.25 mm; they were imaged at a rate of 1 frame per second. The images were processed with Vic-3D using a correlation subset of 29×29 pixels, and the strain field was computed from an 8-tap B-sline interpolation of the displacement field (Sutton et al. 2009). The slit was made with a scalpel and had a length $2a = 2$ mm, and the initial length of the slit, measured in pixels, provided a calibration factor.

Two types of tests were carried out: uniaxial tests on 12.7-mm-wide (ASTM D-412 A) dogbone samples aligned with the machine direction of the film, and biaxial tests on spherical bubbles obtained by inflating a flat circular sample with diameter of 125 mm, clamped around the edge. Both sets of samples contained a 2-mm-wide slit in the middle. In the first test, the machine direction of the film was aligned with the loading direction. The second test used an air pressure box with a 125-mm-diameter hole; see Fig. 8. StratoFilm samples were clamped over the box, and the box was connected to an Omega IP610-030 pressure regulator. The applied pressure was measured with an Omega DPG409-015G electronic pressure gauge. The deformed shape of the test sample was measured with DIC, and the strain field near the crack was obtained with Vic-3D using the same settings as described before. Air leakage through the slit was prevented by means of an inner layer of wrap foil liner. According to a preliminary FEM analysis of the inflation of the film, the maximum stress occurs in the middle of the bubble, and hence the slit was placed there.

All tests were performed at 253 K, starting half an hour after closing the door of the environmental chamber and setting the controller at this temperature.

Author's personal copy

Fig. 7 Instron thermal chamber with DIC cameras

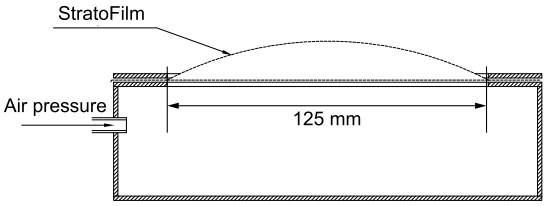

Fig. 8 Section of pressure box for biaxial tests

The next sections discuss how the strain fields obtained from Vic3D were used to compute the stress in the film using the constitutive model presented in Sect. 2.2. Then the results of the J-integral calculation and the critical value J_c are presented for each experiment.

5 Calculation of stress components and strain energy

The Green–Lagrange strains near the crack region of each sample, obtained from DIC at regular time steps, were used to compute the corresponding second Piola–Kirchhoff stresses. The large-strain viscoelastic model presented in Sect. 2.2 was used.

The calculation of the stress components is analogous to the one-dimensional case summarized in Sect. 2.1, with a few additional details to account for the change to three dimensions. Equation (8) is replaced by

$$d\epsilon_{jki} \cdot \left(E_i^{jklm} + \frac{\mu_i^{jklm}}{dt} \right) - \sigma_t^{lm} = -\epsilon_{jki\,t-1} \cdot E_i^{jklm}, \tag{21}$$

Author's personal copy

and Eq. (9) by

$$d\epsilon_{jk0t} + \sum_{i=0}^{n} d\epsilon_{jkit} = \epsilon_{jkt} - \epsilon_{jk0t-1} - \sum_{i=0}^{n} \epsilon_{jkit-1}. \tag{22}$$

In a general 3D situation, Eqs. (21)–(22) provide $6(n+1)$ independent equations. However, in a thin film, $\sigma_{33} = 0$, $\sigma_{23} = 0$, and $\sigma_{13} = 0$. Although the through-thickness strain components are not measured, ϵ_{33} appears in the model and hence is required for the analysis.

Consider the time-independent part of the constitutive model for a viscoelastic thin film that is loaded in-plane. For a general element i of the Prony series, neglecting to show the subscript i for simplicity, the stiffness equations have the form

$$\begin{bmatrix} E_{11} & E_{12} & E_{13} & 0 & 0 & 0 \\ E_{12} & E_{22} & E_{23} & 0 & 0 & 0 \\ E_{13} & E_{23} & E_{33} & 0 & 0 & 0 \\ 0 & 0 & 0 & E_{44} & 0 & 0 \\ 0 & 0 & 0 & 0 & E_{55} & 0 \\ 0 & 0 & 0 & 0 & 0 & E_{66} \end{bmatrix} \cdot \begin{bmatrix} \epsilon_{11} \\ \epsilon_{22} \\ \epsilon_{33} \\ \epsilon_{23} = 0 \\ \epsilon_{13} = 0 \\ \epsilon_{12} \end{bmatrix} = \begin{bmatrix} \sigma_{11} \\ \sigma_{22} \\ \sigma_{33} = 0 \\ \sigma_{23} = 0 \\ \sigma_{13} = 0 \\ \sigma_{12} \end{bmatrix}, \tag{23}$$

where all out-of-plane stress components are zero as shown on the right-hand side of the equation. Only the shear part of the stiffness matrix is diagonal because the material is orthotropic. Since the out-of-plane shear stresses are zero, the corresponding shear strains are also zero, but note that $\epsilon_{33} \neq 0$.

The constitutive equations can also be written in terms of compliance:

$$\begin{bmatrix} D_{11} & D_{12} & D_{13} & 0 & 0 & 0 \\ D_{12} & D_{22} & D_{23} & 0 & 0 & 0 \\ D_{13} & D_{23} & D_{33} & 0 & 0 & 0 \\ 0 & 0 & 0 & D_{44} & 0 & 0 \\ 0 & 0 & 0 & 0 & D_{55} & 0 \\ 0 & 0 & 0 & 0 & 0 & D_{66} \end{bmatrix} \cdot \begin{bmatrix} \sigma_{11} \\ \sigma_{22} \\ \sigma_{33} = 0 \\ \sigma_{23} = 0 \\ \sigma_{13} = 0 \\ \sigma_{12} \end{bmatrix} = \begin{bmatrix} \epsilon_{11} \\ \epsilon_{22} \\ \epsilon_{33} \\ \epsilon_{23} = 0 \\ \epsilon_{13} = 0 \\ \epsilon_{12} \end{bmatrix}, \tag{24}$$

where three stress components and two strain components are zero as before.

The third equation in Eq. (24) can be used to obtain an expression for ϵ_{33} in terms of σ_{11} and σ_{22}:

$$\epsilon_{33} = D_{13} \cdot \sigma_{11} + D_{23} \cdot \sigma_{22}. \tag{25}$$

Then, substituting Eq. (25) into the first two equations in Eq. (23) we obtain:

$$\begin{bmatrix} E_{11} & E_{12} & E_{13} \\ E_{12} & E_{22} & E_{23} \end{bmatrix} \cdot \begin{bmatrix} \epsilon_{11} \\ \epsilon_{22} \\ D_{13}\sigma_{11} + D_{23}\sigma_{22} \end{bmatrix} = \begin{bmatrix} \sigma_{11} \\ \sigma_{22} \end{bmatrix}. \tag{26}$$

Rearranging these equations yields

$$\begin{bmatrix} E_{11} & E_{12} \\ E_{12} & E_{22} \end{bmatrix} \cdot \begin{bmatrix} \epsilon_{11} \\ \epsilon_{22} \end{bmatrix} = \begin{bmatrix} 1 - E_{13}D_{13} & -E_{13}D_{23} \\ -E_{23}D_{13} & 1 - E_{23}D_{23} \end{bmatrix} \cdot \begin{bmatrix} \sigma_{11} \\ \sigma_{22} \end{bmatrix}, \tag{27}$$

and inverting yields

$$\begin{bmatrix} 1 - E_{13}D_{13} & -E_{13}D_{23} \\ -E_{23}D_{13} & 1 - E_{23}D_{23} \end{bmatrix}^{-1} \cdot \begin{bmatrix} E_{11} & E_{12} \\ E_{12} & E_{22} \end{bmatrix} \cdot \begin{bmatrix} \epsilon_{11} \\ \epsilon_{22} \end{bmatrix} = \begin{bmatrix} \sigma_{11} \\ \sigma_{22} \end{bmatrix}, \tag{28}$$

Author's personal copy

which can be written in the form

$$\begin{bmatrix} E^*_{11} & E^*_{12} \\ E^*_{12} & E^*_{22} \end{bmatrix} \cdot \begin{bmatrix} \epsilon_{11} \\ \epsilon_{22} \end{bmatrix} = \begin{bmatrix} \sigma_{11} \\ \sigma_{22} \end{bmatrix}, \tag{29}$$

where the coefficients of the 2D stiffness matrix are obtained from the matrix product in Eq. (28).

Since the viscoelastic model in Sect. 2.2 has been given in terms of compliance coefficients, the 2D stiffness matrix in Eq. (29) is obtained by inversion of the 2×2 compliance matrix obtained by removing rows and columns from Eq. (24).

After calculating all the coefficients of the Prony series for the relaxation modulus, the 2D version of Eqs. (21) and (22) is as follows:

$$d\epsilon_{jki} \cdot \left(E_i^{*jklm} + \frac{\mu_i^{*jklm}}{dt} \right) - \sigma_t^{lm} = -\epsilon_{jkit-1} \cdot E_i^{*jklm}, \tag{30}$$

$$d\epsilon_{jk0t} + \sum_{i=0}^{n} d\epsilon_{jkit} = \epsilon_{jkt} - \epsilon_{jk0t-1} - \sum_{i=0}^{n} \epsilon_{jkit-1}, \tag{31}$$

where $j, k, l, m = (1, 2)$.

The system of $2(n + 1)$ equations provided by Eqs. (30) and (31) is solved at each time step to obtain the stress time history from the measured strain history.

Once the stress components $\sigma_{11t}, \sigma_{22t}, \sigma_{12t}$ have been obtained, ϵ_{33} is calculated from (Kwok and Pellegrino 2011; Kwok 2012)

$$\epsilon_{33t} = D_{13t} \cdot \sigma_{11t} + D_{23t} \cdot \sigma_{22t} - f_{33t-\Delta t}, \tag{32}$$

where $f_{t-\Delta t}$ is the hereditary parameter investigated by Lai and Bakker (1996):

$$f_{33t-\Delta t} = \sum_{i=1}^{n} D_{ijk} \left(e^{-\Delta t'/\tau_i} \cdot q_{ijkt-\Delta t} - \frac{1 - e^{-\Delta t'/\tau_i}}{\Delta t'/\tau_i} \right), \tag{33}$$

and

$$q_{ijkt} = e^{-\Delta t'/\tau_i} \cdot q_{ijkt-\Delta t} - (\sigma_{jkt} - \sigma_{jkt-\Delta t}) \frac{1 - e^{-\Delta t'/\tau_i}}{\Delta t'/\tau_i}. \tag{34}$$

The final step in the analysis is the calculation of the elastic strain energy density and the dissipated energy density at each time step. The elastic strain energy density is given by

$$W_t^E = \sum_{i=0}^{n} \epsilon_{ijkt} \cdot E^{jklm} \cdot \epsilon_{it}^{lm}. \tag{35}$$

Hence, the dissipated energy density is calculated as the difference between the total work done and the strain energy density from Eq. (35). The total work is given by

$$W_t = \sum_{i=0}^{n} \epsilon_{ijkt} \cdot \sigma_{it}^{jk}. \tag{36}$$

The accuracy of this procedure has been confirmed for each uniaxial test by generating a "control plot." These plots, shown in Fig. 9, include the longitudinal average strain, obtained from the strain measured along a transverse cross section located far away from the slit, and the measured stress, obtained by dividing the applied force by the initial cross-sectional area of the test sample and without considering the cross-sectional area reduction due to the slit during the full duration of a particular uniaxial test. They also include the average computed stress in the sample, obtained from the average strain described above, at a distance of 12 to 15 mm from the slit. The stress values were derived from the strain field measured with DIC and were converted to stress using the constitutive model.

Author's personal copy

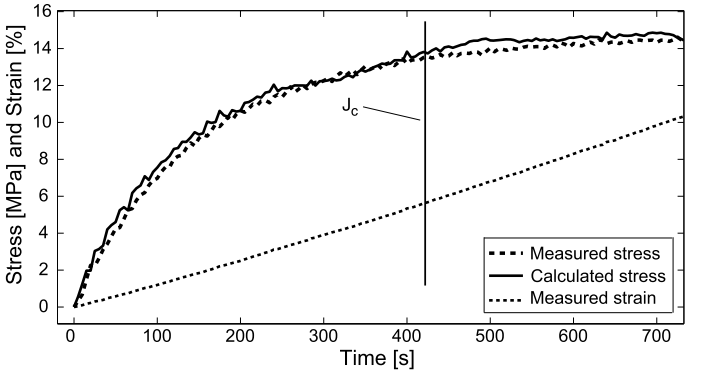

(a)

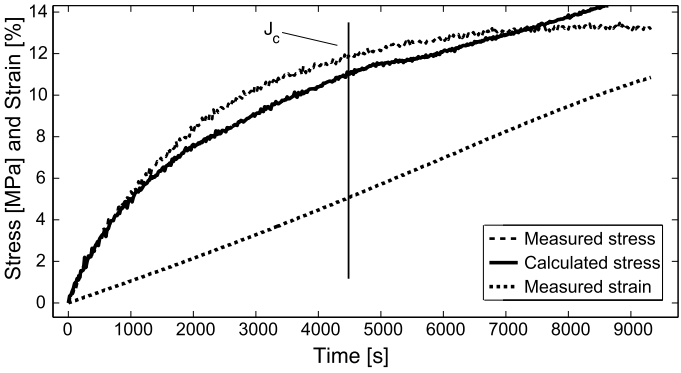

(b)

Fig. 9 Control plots showing average longitudinal stress and strain in dogbone sample far away from the slit. The tests were carried out at 253 K and rates of (**a**) 1.33×10^{-4} s^{-1} and (**b**) 1.33×10^{-5} s^{-1}

6 *J*-integral diagrams

The calculation of the J-integral along a chosen path Γ, Eq. (18), requires the strain energy and the stress components to be known along the path. The path Γ is chosen far from the slit to avoid regions of high strain where the onset of plasticity may invalidate the constitutive model. Note that Γ is required to intersect the edge of the slit (see Fig. 5), but the interpolation functions used in standard DIC cannot measure strains close to a free edge. Fortunately, in the present case, the strain and stress magnitudes near the slit edges are relatively small, provided that Γ does not get too close to the tips of the slit and the length of the omitted integration line is relatively short compared to the total length of Γ.

For each test, the J-integral was calculated along an approximately elliptical path with a horizontal semiaxis approximately 4-mm long and vertical semiaxis approximately 6-mm long; see Fig. 10. Note that for the example shown in this figure, the maximum longitudinal strain component along the chosen path is < 5 %, which is well below the limit of validity of the large-strain viscoelastic model. The calculation was repeated for each time step, and the results are shown for each test by means of two different types of plots. The first is the standard plot of J vs. Δa, defined as the change in distance between the two opposite ends of the tear, and the second is a plot of J vs. the $Area$ enclosed by the slit. Because in soft

Author's personal copy

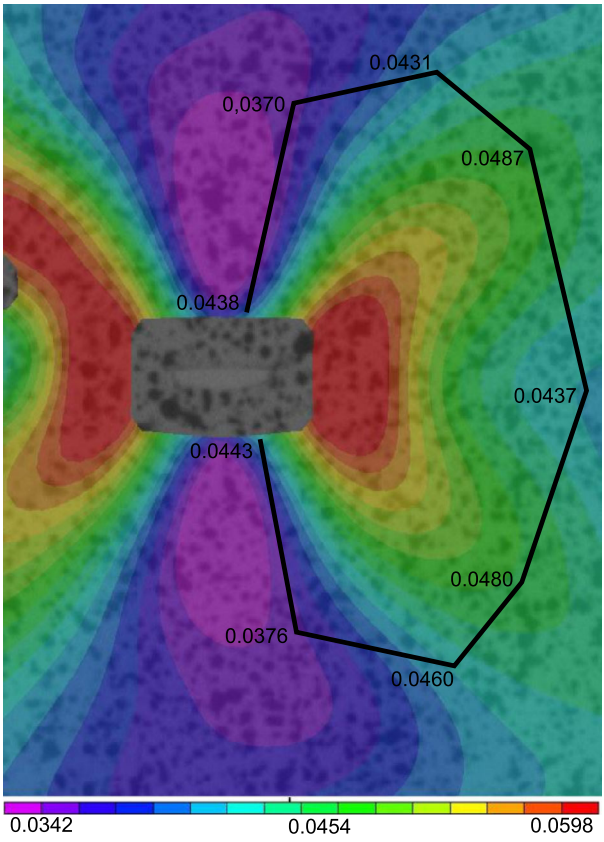

Fig. 10 Normal strain components in vertical direction around the slit, from uniaxial test at $T = 253$ K at a rate of 1.33×10^4 s^{-1}. The *rounded rectangle at the center* has been excluded from the strain calculation

and highly ductile materials, such as LLDPE film, it is sometimes difficult to identify the onset of crack propagation only from the plot of J vs. Δa, the second plot is in some cases useful to better find the critical value of J. Here, *Area* is an additional parameter that better takes into account the expansion of the slit in the direction perpendicular to the original slit direction. The slit was assumed to be elliptical in shape, and its area was obtained by measuring the two axes of the ellipse and computing the resulting area. Both diagrams were used to identify J_c, as explained later on.

The value of the J-integral has been computed from experimentally obtained data around the tips of the tear, denoted as A-side and B-side; both the elastic strain energy density (obtained from Eqs. (35) and (36)) and the total work are plotted. The reason why the J-integral on both the A- and B-sides is needed is because a small asymmetry in the test arrangement or variability in the film thickness or material properties leads to more energy being accumulated on one side and then the tear propagates asymmetrically. Typically, the start of the propagation on one side will trigger propagation also on the other side, but the critical value of the J-integral is associated with the more heavily strained side.

To understand the J-integral plots presented in this section, consider the idealized diagram of J vs. Δa in Fig. 5. This diagram consists of a vertical line, corresponding to an accumulation of the deformation energy around the tear, followed by a smooth curve with finite initial slope. The point at the top of the line, labeled C, marks the sudden prop-

Author's personal copy

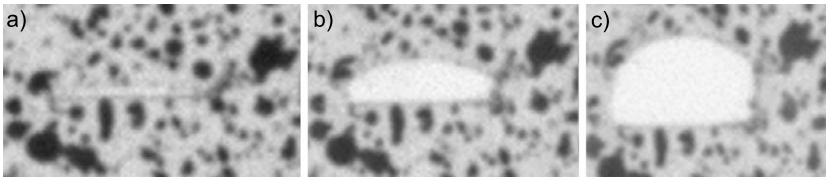

Fig. 11 (**a**) Initial tear, (**b**) blunted tear begins to propagate, and (**c**) propagating tear for uniaxial test at 253 K and 1.33×10^{-4} s^{-1}

agation of the tear. Point C corresponds to a sudden decrease in the rate of energy accumulation and a sudden increase in the expansion of the tear; it corresponds to the critical value J_c. In viscoplastic materials, this transition is less sharp, as shown in Fig. 11. The tear blunting phase has the effect of shifting the vertical line since local deformation in the tip region causes the tear length to vary during the accumulation phase. In thin films, the situation is even more complicated since additional shifting of the originally vertical line may be caused by wrinkling of the film. In such cases, the J vs. Δa diagram may turn back since the tear appears to become shorter and thus no longer lies in a plane. The alternative plot of J vs. $Area$ is useful in resolving situations where the main plot is confusing.

In all cases, though, the transition from the accumulation phase to the propagation phase is defined by an inflection point in the experimentally obtained data, and hence point C in the J-integral curve was determined by carrying out successive polynomial fits and looking for a sign-change in the second-order coefficient. Figures 12 and 13 present representative results from uniaxial tests respectively at faster and slower rates. For the faster test, the point of inflection C is clearly visible in the plot of J vs. Δa in Fig. 12(a); the critical value is $J_c = 700$ J/m^2. Note that in this case, finding point C in the area plot, Fig. 12(b), is harder since the graph shows a region of clearly positive curvature followed by an almost straight trend line. For the slower test, the standard plot, Fig. 13(a), is less clear due to the extensive turn back, whereas the area plot, Fig. 13(b), shows a clear point of inflection; here $J_c = 1100$ J/m^2.

It is interesting to note that in the faster test, Fig. 12, there is practically no difference between elastic strain energy and total work, whereas in the slower test, Fig. 13, the difference is clearly visible and is on the order of 20 % of J_c.

The accuracy of the constitutive model at the time at which the tear began to propagate in the two uniaxial tests can be assessed from the control plots. It can be seen from these plots, shown in Fig. 9, that the stress estimate is better than 10 % in correspondence of J_c.

Figures 14 and 15 present results from two bubble tests. In this type of test, only the pressure rate is controlled, not the strain rate. The test presented in Fig. 14 had a much faster pressure rate (on the order of 50 times faster) than the test presented in Fig. 15. For the first test, both of the J-integral plots presented in Fig. 14 are quite clear, although the point of inflection is particularly clear in Fig. 14(b), from which $J_c = 750$ J/m^2. For the second test, Fig. 15, the plot of J vs. Δa shows an initial region of clearly positive curvature followed by a region of (rather small) negative curvature; hence, we obtain $J_c = 1300$ J/m^2 from this plot. The plot of J vs. $Area$, Fig. 15(b), follows an almost straight line, making it difficult to spot J_C. Note that in Figs. 14 and 15, there is practically no difference between stored strain energy and total work, probably because the local strain rate was at least as high as in the first uniaxial test.

Author's personal copy

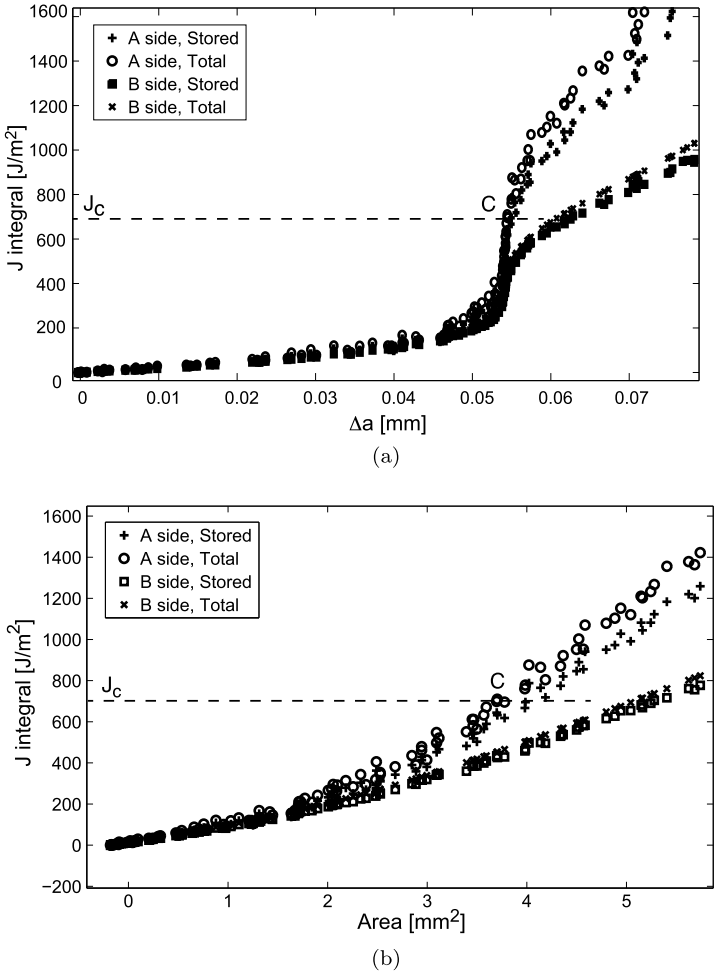

Fig. 12 Variation of J-integral with (**a**) tear length change and (**b**) tear enclosed area for uniaxial test at 253 K and 1.33×10^{-4} s^{-1}

7 Discussion and conclusion

The objective of this study was to establish a simple and direct technique to obtain the critical values of the J-integral for Stratofilm 420 from direct measurements.

A 2-mm-wide central slit perpendicular to the direction of loading in a 12.7-mm-wide by 75-mm-long dogbone sample was found the best initial defect to trigger failure in a known region of the sample while also avoiding widespread plastic deformation. Tear propagation experiments were carried out with two test configurations, namely the uniaxially loaded dogbone sample already described before, and a flat circular diaphragm with diameter of 125 mm and a central 2-mm-wide slit. This sample was inflated into a spherical bubble by applying a uniform pressure loading. A standard 3D DIC experimental setup was used to measure the strain field in the tear region, and the large-strain viscoelastic

Author's personal copy

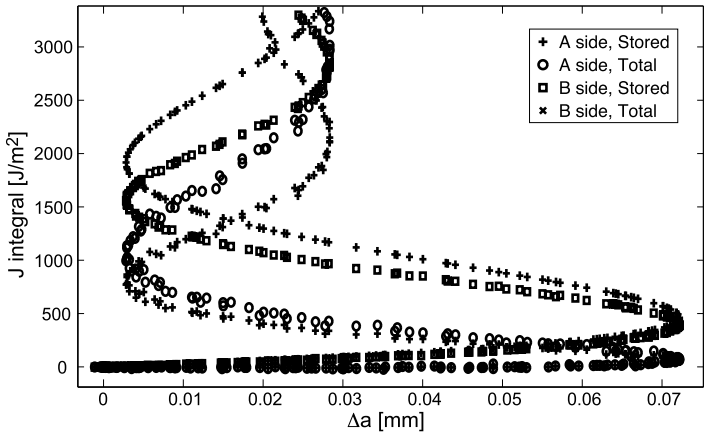

(a)

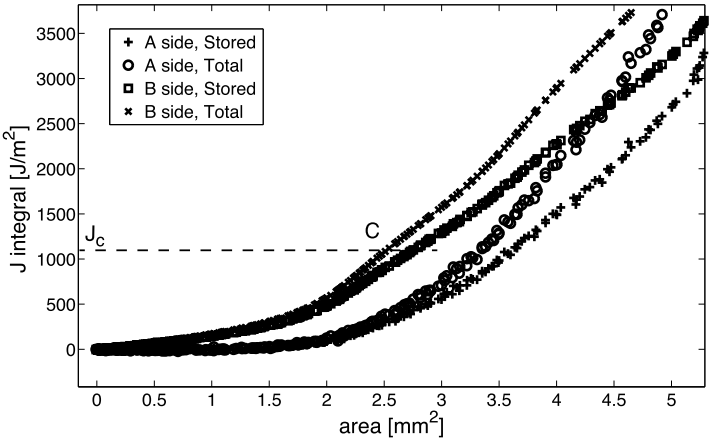

(b)

Fig. 13 Variation of J-integral with (**a**) tear length change and (**b**) tear enclosed area for uniaxial test at 253 K and 1.33×10^{-5} s^{-1}

model summarized in Sect. 2.2 was used to compute the corresponding time-dependent stress fields.

We found that the large-strain viscoelastic model provides predictions of the average stress across the dogbone samples, accurate to better than 10 % at the point where the critical value of J is reached.

From these stress and strain fields we evaluated the J-integral along closed paths that surround each end of the tear, and thus we were able to construct plots of the J-integral vs. two different measurements of the tear, namely the tear length and the enclosed area. Some of these plots did not show a clear transition from the initial phase, involving the accumulation of strain energy in the region surrounding the tear, to the second phase, involving propagation of the tear through the film. However, for each test, at least one type of plot provided conclusive information from which the critical value of the J-integral could be evaluated.

Author's personal copy

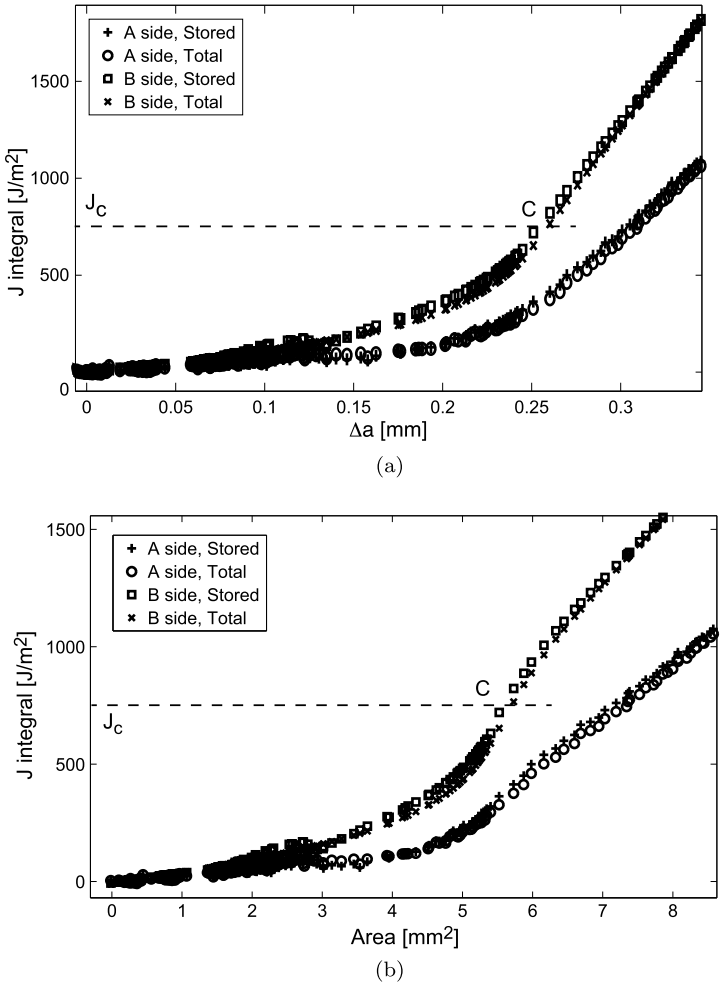

Fig. 14 Variation of J-integral with (**a**) tear length change and (**b**) tear enclosed area for bubble test #1 at 253 K

The effects of the film orthotropicity, although accounted for in the material model, were not investigated in detail.

The resulting values of J_c, all obtained at a temperature of 253 K, were 700 J/m^2 and 1100 J/m^2, respectively, for strain rates of 1.33×10^{-4} s^{-1} and 1.33×10^{-5} s^{-1}.

The values of J_c obtained from bubble tests, in which the strain rate cannot be controlled directly, were 750 J/m^2 and 1300 J/m^2 in the faster and slower tests, respectively. These values closely match the values from uniaxial tests, suggesting that the simpler test configuration could be used in the future for more extensive studies of strain-rate and temperature sensitivity of the tearing of StratoFilm.

It is concluded thats the approach investigated in this paper appears to capture the combination of nonlinear effects (time dependency, plasticity, wrinkling) that occur near a tear in a thin film.

Author's personal copy

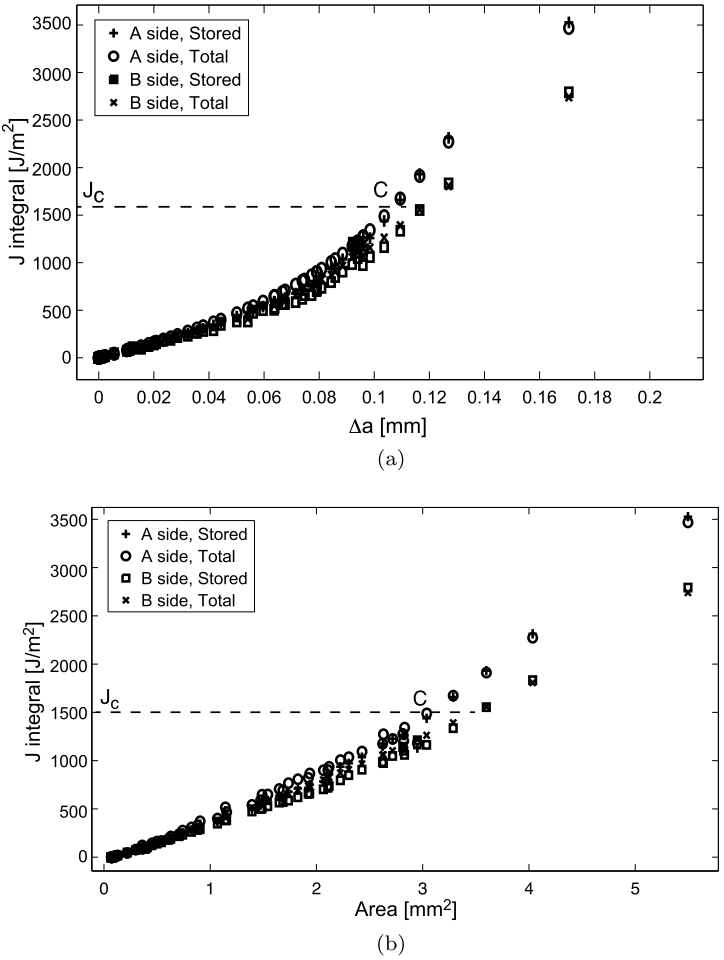

Fig. 15 Variation of J-integral with (**a**) tear length change and (**b**) tear enclosed area for bubble test #2 at 253 K

Acknowledgements We thank Prof. Wolfgang Knauss, Dr. Kawai Kwok, and Dr. Jun Li for helpful comments and advice. DH research at the California Institute of Technology was supported by an Imre Koranyi Civil Engineering Fellowship from the Thomas Cholnoky Foundation. Financial support from the NASA Balloon Research Program is gratefully acknowledged.

References

Begley, J.A., Landes, J.D.: The J integral as a fracture criterion. ASTM STM **515**, 1–23 (1972)

Brinson, H.F.: Matrix dominated time dependent failure prediction in polymer matrix composites. Compos. Struct. **47**, 445–456 (1999)

Brinson, H.F., Brinson, L.C.: Polymer Engineering Science and Viscoelasticity. Springer, Berlin (2008)

Brown, B., Lu, X.: A fundamental theory for slow crack growth in polyethylene. Polymer **36**(3), 543–548 (1995)

Bruler, O.S.: The energy balance of a viscoelastic material. Int. J. Polym. Mater. **2**, 137–148 (1973)

Bruler, O.S.: The energy balance of a viscoelastic material. Int. J. Polym. Mater. **21**(3), 145–150 (1981)

Author's personal copy

Chan, W.Y.F., Williams, J.G.: Determination of the fracture toughness of polymeric films by the essential work method. Polymer **35**(8), 1666–1672 (1994)
Christensen, R.M.: Theory of Viscoelasticity: An Introduction, 2nd edn. Academic Press, New York (1982)
Coleman, B.D., Noll, W.: Foundations of linear viscoelasticity. Rev. Mod. Phys. **33**, 239–249 (1961)
Crochet, M.J.: Symmetric deformations of viscoelastic-plastic cylinders. J. Appl. Mech. 327–334 (1966)
Ferry, J.D.: Viscoelastic Properties of Polymers, 3rd edn. Wiley, New York (1980)
Flugge, W.: Viscoelasticity. Springer, New York (1975)
Knauss, W.: Time dependent fracture of polymers. In: Advances in Fracture Research: Proceedings of the 7th International Conference on Fracture (ICF-7), Houston, Texas, 20–24 March 1989. International Series on the Strength and Fracture of Materials and Structures, vol. 4, pp. 2683–2711. Pergamon Press, New York (1989)
Knauss, W.G., Emri, I.J.: Nonlinear viscoelasticity based on free volume consideration. Comput. Struct. **13**, 123–128 (1981)
Knauss, W.G., Emri, I.J.: Volume change and the nonlinearly thermo-viscoelastic constitution of polymers. Polym. Eng. Sci. **27**, 86–100 (1987)
Kwok, K.: Mechanics of viscoelastic thin-walled structures. PhD thesis, Caltech (2012)
Kwok, K., Pellegrino, S.: Large strain viscoelastic model for balloon film. In: 11th AIAA ATIO Conference, Virginia Beach, 20–22 September 2011, AIAA-2011-6939 (2011)
Lai, J., Bakker, A.: 3-d Schapery representation for nonlinear viscoelasticity and finite element implementation. Comput. Mech. **18**, 182–191 (1996)
Li, J., Kwok, K., Pellegrino, S.: Large-strain thermoviscoelastic models for polyethylene thin films. Mech. Time-Depend. Mater. (2015, submitted)
Naghdi, P.M., Murch, S.A.: On the mechanical behavior of viscoelastic/plastic solids. J. Appl. Mech. 321–328 (1963)
Rand, J.L.: An improved constitutive equation for SF420. Winzen Engineering (2008)
Rand, J.L., Wakefield, D.: Studies of thin film nonlinear viscoelasticity for superpressure balloons. Adv. Space Res. **45**, 56–60 (2010)
Rice, J.R., Rosengren, G.F.: Plane strain deformation near a crack tip in a power-law hardening material. J. Mech. Phys. Solids **16**, 1–12 (1968)
Sutton, M.A., Orteu, J.J., Schreier, H.W.: Image Correlation for Shape, Motion and Deformation Measurements: Basic Concepts, Theory and Applications. Springer, Berlin (2009)
Tielking, J.T.: A fracture toughness test for polymer film. Polym. Test. **12**, 207–220 (1993)
Williams, M.L., Landel, R.F., Ferry, J.D.: The temperature dependence of relaxation mechanisms of amorphous polymers and other glass-forming liquids. J. Am. Chem. Soc. **77**, 3701–3707 (1955)
Young, L.: CTE curve fitting data. NASA Balloon Program Office Report (2010)